Journal of Materials Chemistry A

Accepted Manuscript

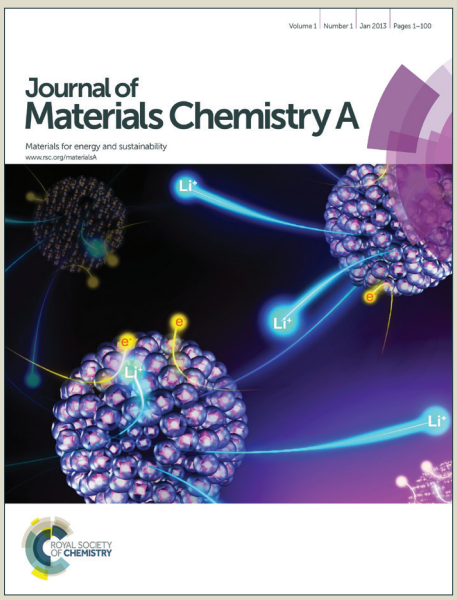

ROYAL SOCIETY OF CHEMISTRY

www.rsc.org/materialsA

Enhanced visible light photocatalytic activity of bismuth oxybromide lamellas with decreasing lamella thicknesses

Haiping Li[a,b], Jingyi Liu[c], Xuefeng Liang[d], Wanguo Hou[a,e]*, Xutang Tao[b]

[a] *National Engineering Technology Research Center for Colloidal Materials, Shandong University, Jinan 250100, P.R. China;*

[b] *State Key Laboratory of Crystal Materials, Shandong University, Jinan 250100, P.R. China;*

[c] *Environment Research Institute, Shandong University, Jinan 250100, P.R. China;*

[d] *Key Laboratory of Original Environmental Quality of MOA, Agro-Environmental Protection Institute of Ministry of Agriculture, Tianjin, 300191, P.R. China;*

[e] *Key Laboratory for Colloid and Interface Chemistry (Ministry of Education), Shandong University, Jinan 250100, P.R. China.*

[*] To whom correspondence should be addressed

Email: wghou@sdu.edu.cn

Telephone: +86-0531-88365460

Fax: +86-0531-88364750

Running title: Enhanced photoactivity of BiOBr lamellas

Abstract

BiOBr lamellas were synthesized at different reaction pH values via a hydrothermal process. X-ray diffraction, scanning electron microscopy, transmission electron microscopy, X-ray photoelectron spectroscopy, UV-vis diffuse reflectance spectroscopy and N_2 sorption measurements were used to characterize the BiOBr samples. BiOBr samples have the same lamella structures and band gaps, but different lamella sizes and thicknesses. Adjusting the pH of the reaction system tunes the BiOBr lamella thickness from 42 to 21 nm. The photodegradation efficiencies of the BiOBr lamellas for rhodamine B (RhB) and methylene blue (MB) in aqueous solution were examined. The degradation efficiency for RhB is much higher than that for MB. The decrease in BiOBr lamella thickness significantly enhances the photocatalytic activity for the dye degradation, despite the decrease in exposed photoactive (001) facet percentage. Decreasing the lamella thickness from 42 to 21 nm yields a more than fourfold enhancement in photodegradation efficiency of BiOBr samples for RhB. The most important factor influencing the photocatalytic activity of the BiOBr samples is their lamella thickness, rather than the exposed (001) facet percentage. Thus, even for flaky semiconductors with high exposed photoactive facet contents, the influence of lamella thickness on photocatalytic activity should be preferentially considered.

Keywords: BiOBr, lamella, nanosheet, thickness, photocatalysis

1. Introduction

Photocatalytic degradation is one of the most effective energy-saving solutions to environmental pollution. Nanometer-scale semiconductors are promising photocatalysts for this goal[1, 2]. Many factors influence the activity of these photocatalysts, such as band gap[3], particle size[4], specific surface area[5] and surface morphology[6, 7]. The surface structures of photocatalysts largely affect their photocatalytic reactions, since reaction is caused by photoinduced electrons and holes on the surface[6, 7].

The facet-dependent photocatalytic activity of semiconductors has received much recent interest[8-22]. Crystalline semiconductors with a high percentage of photoactive facets can function better than those with lower contents. Many semiconductors have been prepared with high percentages of exposed photoactive facets. Kuang et al. synthesized TiO_2 nanosheets and hollow TiO_2 boxes with high percentages of exposed (001) facets, and found that the TiO_2 samples with a higher percentage of (001) facets exhibited higher catalytic activity in the degradation of methyl orange (MO)[15] and splitting water[19]. Ye et al. prepared single-crystalline Ag_3PO_4 rhombic dodecahedrons with only (110) facets exposed, and cubes bounded entirely by (100) facets[17]. The rhombic dodecahedrons exhibited much higher activities than the cubes for the degradation of MO and rhodamine B (RhB), which was attributed to the higher surface energy of (110) facets. Wu et al. synthesized high (001) facet content BiOBr lamellas without capping agents, and found that higher (001) facet contents led to enhanced photodegradation efficiencies for RhB and MO[8]. BiOI[9], BiOCl[18], BiVO4[10], Bi_2O_3[23] and Bi_2MoO_6[11] with high percentages of exposed (001), (001), (001), (001) and (010) facets, respectively, also exhibit high photocatalytic activities. However, such reports investigating the influence of active facet percentage on the photoactivity have usually neglected the effects of other factors such as particle size, specific surface area and morphology. It is usually difficult to retain a constant particle size, specific surface area or

morphology when exposing more photoactive facets. Thus, this should be considered when exploring the influence of active facet percentage on photoactivity.

Bismuth oxyhalides (BiOX, where X = Cl, Br or I) are a new family of visible light-driven photocatalysts. They have attracted much attention because of their structure-dependent photocatalytic performance, which arises from their layered structure interleaved with $[Bi_2O_2]^{2+}$ and double halogen atom slabs[8, 9, 24, 25]. The layered structure benefits the separation of photoinduced electrons and holes under the effect of an internal electric field between $[Bi_2O_2]^{2+}$ and halogen layers[24], and also the relatively large distortion of the B–O polyhedron[9, 11]. BiOBr has a desirable band gap (~2.7 eV) for visible light adsorption[24, 26]. BiOBr reportedly has two separate valence bands, which have different oxidation abilities and respond to UV and visible light, respectively[27]. To enhance its photocatalytic activity, BiOBr has been prepared with various morphologies such as hierarchical flower-like microspheres[28, 29], hollow microspheres[30] and lamellas with a high percentage of exposed (001) facets[8]. Photocatalytic activity has also been enhanced by combining BiOBr with other elements to form solid solutions[31], or with compounds to form heterostructures[32]. To our knowledge, the influence of lamella thickness of BiOBr nanosheets on their photocatalytic efficiency has not been systematically investigated.

In the current study, a series of BiOBr lamellas were synthesized via a hydrothermal route[24, 33, 34]. The lamella size, especially the lamella thickness, of BiOBr samples was adjusted by changing the pH of the reaction systems. The BiOBr lamella samples have specific surface areas (S_{BET}) within one order of magnitude and similar band gaps, but different lamella thicknesses and percentages of exposed active (001) facets (F_{001}). The dependence of photocatalytic activity on BiOBr sample thickness and F_{001} were examined, to distinguish which factors are the most important in improving photocatalytic performance.

2. Experimental

2.1. Materials

$Bi(NO_3)_3 \cdot 5H_2O$, hexadecyltrimethylammonium bromide (CTAB), NaOH, RhB, MB and ethanol were of A.R. grade, and were purchased from Sinopharm Chemical Reagent Co., Ltd. (Shanghai, P. R. China) and used without further purification. Commercial N doped anatase TiO_2 (N-TiO_2) with N content of about 4% was purchased from Xuan Cheng Jing Rui New Material Co., Ltd. Water used in experiments was obtained from a Hitech-Kflow water purification system (Hitech, Shanghai, P. R. China).

2.2. Synthesis of BiOBr crystals

BiOBr lamellas were synthesized as reported with minor modifications[24, 33, 34]. Specifically, 9.0 g of $Bi(NO_3)_3 \cdot 5H_2O$ and 9.0 g of CTAB were dissolved in 450 mL water by stirring for 10 min. The dispersion was divided equally into six parts. The initial pH of these dispersions was about 1.4. Aqueous NaOH (1 mol/L) was added dropwise to five of the dispersions, to adjust their pH values to 2.0, 3.0, 4.0, 5.0 and 7.0, respectively. The resulting dispersions were stirred for 1 h at room temperature, then transferred into 100-mL autoclaves and heated at 160 °C for 18 h. Finally, the precipitates were collected by filtration, washed thoroughly with water and ethanol, and dried at 60 °C in an oven. The BiOBr lamella samples obtained at pH values of 1.4, 2.0, 3.0, 4.0, 5.0 and 7.0 were denoted as H1.4, H2, H3, H4, H5 and H7, respectively.

2.3. Characterization

Powder X-ray diffraction (XRD) was carried out using a D8 Advance diffractometer (Bruker, Germany), with Cu Kα radiation (λ = 1.54184 Å). UV-vis diffuse reflectance spectra (UV-vis DRS) were obtained on a Cary 100 spectrophotometer (Agilent, USA), with a $BaSO_4$ reference. X-ray photoelectron spectroscopy (XPS) was performed on a Phi 5300 esca system (Perkin-Elmer, USA), with Mg Kα radiation (photoelectron energy 1253.6 eV). The C 1s peak at 284.6 eV was used to calibrate peak positions. The composite structure was probed with

transmission electron microscopy (TEM), using a JEM-2100F microscope (Jeol, Japan). Morphologies were examined with a Supra55 field emission-scanning electron microscopy (SEM) (Zeiss, USA). Atomic force microscopic (AFM) measurements were performed in air with a Nanoscope IIIa instrument (Digital Instruments Inc., Santa Barbara, CA) operating in the tapping mode (TM). S_{BET} values and pore structures were probed by measuring volumetric N_2 adsorption-desorption isotherms at liquid nitrogen temperature, using an Autosorb IQ-MP instrument (Quantachrome, USA). Samples were degassed at 150 °C for 3 h under vacuum before measurements.

2.4. Photocatalytic activity

The photocatalytic performance of as-prepared catalysts under visible light irradiation was evaluated by the degradation of RhB and MB at room temperature, on a XPA-7 photocatalytic reaction apparatus (Xujiang Electromechanical Plant, Nanjing, P. R. China). A 350 W Xe lamp was used as the light source, and was equipped with an ultraviolet cutoff filter ($\lambda \geq 420$ nm) to provide visible light. The distance between the lamp and glass tubes containing dye solutions was about 10 cm. A water filter around the lamp was used to adsorb infrared light. The reaction tubes around the lamp were soaked in a constant temperature bath. For each run, 0.02 g of photocatalyst was added to 50 mL of RhB (10 mg/L) or MB (5 mg/L) solution. Prior to irradiation, the suspension was treated by ultrasonication for 5 min and then stirred in the dark for 1 h, to ensure sorption equilibrium. After a given irradiation time, ~4 mL aliquots were collected and filtered through 1.0-μm nylon syringe filters. The absorbance of filtrates was measured by a SP-1105 visible spectrophotometer (Shanghai Spectrum Instrument Co., Ltd., P. R. China), at wavelengths of 554 nm for RhB and 664 nm for MB. The ratio of remaining RhB or MB concentration to its initial concentration, C/C_0, was obtained by calculating the ratio of the corresponding absorbance intensity.

3. Results and discussion

3.1. XRD analysis

Fig. 1 shows XRD patterns of the BiOBr samples. The intense and clear diffraction peaks imply good crystallinity of the as-prepared samples. All samples exhibit the same diffraction peak positions. The peaks at 10.9, 22.0, 25.3, 31.8, 32.3, 33.3, 39.4, 44.9, 46.3, 47.0, 50.8, 53.5, 56.4, 57.3, 62.1 and 69.8° correspond to the (001), (002), (011), (012), (110), (003), (112), (004), (020), (113), (014), (211), (114), (212), (015) and (006) planes, respectively, and are indexed as pure tetragonal phase BiOBr (JCPDS file 73-2061, space group: P4/nmm, unit cell parameters: a = 3.923 Å, b = 3.923 Å and c = 8.105 Å). A significant decrease in the relative intensity of the (001), (002), (003), (004) and (006) peaks is observed from H1.4 to H7, as marked with '*' in the figure. This implies a decrease in F_{001} content. The relative intensities of the peaks for H7 match well with those of the standard pattern shown at the bottom of Fig. 1.

The average c-axis crystallite size, D, of the BiOBr samples was calculated from the (001) peak of the XRD pattern using the Scherrer formula:

$$D = \frac{0.9\lambda}{B\cos\theta} \quad (1)$$

where λ, B and θ are the Cu Kα wavelength, full width at half-maximum intensity in radians, and Bragg diffraction angle, respectively[35]. The results are shown in Table 1. From H1.4 to H7, D initially decreases and then subsequently increases, with a minimum D observed for H4. H1.4 has the largest D of 42 nm. These results demonstrate that the c-axis crystallite size can be controlled through adjusting the pH of the reaction.

3.2. Morphology

The general morphologies of BiOBr samples prepared at different pH values are revealed by SEM (Fig. 2). A flaky structure is apparent for all samples, and their lamella size distributions are shown in Fig. S1 (Supporting Information). The average lamella sizes (L) of the six BiOBr samples are listed in Table 1. From H1.4 to H7, L decreases from 963 to 230

nm and then increases to 554 nm, with H4 exhibiting the lowest *L*. The average lamella thickness (*H*) of H1.4, H2, H4, H5 and H7 is measured to be about 39, 34, 32, 24, 28 and 34 nm, respectively, as shown in the insets in Fig. 2 and in Table 1. *H* and *L* exhibit the same trend from H1.4 to H7. The lamella thickness (H_A) was also measured from AFM images (Fig. S2 in Supporting Information). The obtained H_A values are similar to *D* and *H* (Table 1). H_A exhibits the same trend from H1.4 to H7 as *D* and *H*. Furthermore, the *H* and H_A of every sample are very close to its *D* (Table 1). This indicates that the obtained lamellas are single crystals, and the transverse planes are the (001) plane, which is also confirmed by TEM observation. Fig. 3 shows TEM images of H4, in which a lamella structure is also observed (Fig. 3a). Fig. 3b and c show HRTEM lattice images of crystal planes magnified from Fig. 3a. The interplanar spacings of 0.274 and 0.197 nm match well with the (110) and (020) planes of tetragonal BiOBr (JCPDS file 73-2061), respectively. The selected area electron diffraction (SAED) pattern (Fig. 3d) indicates that the BiOBr nanosheet is a single crystal of high crystallinity. These results indicate that the highly exposed planes of BiOBr lamellas are (001) planes, consistent with published reports[8].

The nanosheet morphology of BiOBr has been widely reported[8, 24, 36]. The formation of BiOBr nanosheets may result from the laminar atomic structure of BiOBr[8]. The unit cell of BiOBr with its tetragonal matlockite-type structure is shown in Scheme 1. One O atom and one Br atom coordinate with four Bi atoms, respectively. One Bi atom coordinates with four O atoms and four Br atoms in different bases, respectively. One $[Bi_2O_2]^{2+}$ layer is sandwiched between two bromine slabs. Different layers are stacked together via weak van der Waals interactions[8, 36]. However, Bi-O bonds are thought to be covalent[37]. Scheme 1 shows that (001) facets are rich in Bi and O atoms. Under irradiation, Bi–O square anti-prisms could generate many oxygen defects because of the unstable bonding between Bi and O[9].

3.3. XPS analysis

The surface chemical composition and structure of H1.4, H4 and H7 were analyzed by XPS. Fig. 4 shows survey scan and high-resolution XPS spectra of the Bi 4f, Br 3d and O 1s regions. The spectra of these three samples exhibit similar peak intensities and binding energies, which indicates that they consist of the same elemental composition and surficial structure. The C 1s peaks in the survey scan spectra result from adventitious carbon[38]. Peaks at 159.3 and 164.6 eV are ascribed to Bi $4f_{7/2}$ and Bi $4f_{5/2}$, respectively, and arise from the Bi-O bonds in BiOBr. The O 1s peaks are fitted by two peaks at 531.4 and 529.9 eV, and are related to oxygen in BiOBr and other components (such as –OH and H_2O) adsorbed on the BiOBr surface, respectively. The peaks at 69.6 and 68.6 eV are attributed to Br $3d_{3/2}$ and Br $3d_{5/2}$, respectively[28]. These XPS results are consistent with previously reported results[28].

3.4. Photocatalytic activity

The visible light photocatalytic activity of the as-prepared BiOBr samples was evaluated for the degradation of RhB and MB in aqueous solutions (Fig. 5). For all tested photocatalysts, adsorption equilibrium is reached after stirring for 1 h in the dark (Figs. S3 and S4 in Supporting Information). The RhB and MB solutions were irradiated with visible light for 160 and 450 min, respectively, in the absence of catalyst, and little change in dye concentrations was observed. This indicates that the photodegradation of RhB and MB in the absence of catalyst is negligible[8, 39]. The photocatalytic activities of these BiOBr samples are quite different, despite their similar lamella structures. From H1.4 to H7, the photocatalytic activity gradually enhances and then decreases, with H4 exhibiting the highest activity (Fig. 5a and 5b). N-TiO_2 exhibits a low photocatalytic efficiency. The total photoactivity follows the sequence H4 > H5 > H7 > H3 > H2 > H1.4 > N-TiO_2. After irradiation for 100 min, about 99% of RhB is degraded by H4 sample, while less than 50% and 15% are degraded by H1.4 and N-TiO_2, respectively (Fig. 5a).

To quantitatively investigate the reaction kinetics of RhB photodegradation by the BiOBr

samples, the experimental data were fitted to the pseudo-first-order model, as expressed by the equation (2):

$$-\ln(C / C_0) = kt \quad (2)$$

where k is the apparent first-order rate constant. As shown in Fig. 5c, all plots of -ln(C/C_0) against t exhibit linear trends, indicating that RhB photodegradation is well described by the pseudo-first-order model. The k values for RhB degradation by H1.4, H2, H3, H4, H5 and H7 are 0.007, 0.010, 0.017, 0.036, 0.030 and 0.020 min^{-1} (Table 1), respectively. The k value of H4 is more than four times larger than that of H1.4 (Table 1). S_{BET} can influence the photocatalytic activity of catalysts. To rule out the effect of S_{BET}, the k values are normalized with respect to S_{BET}[24], and the normalized k for H4 is still more than four times larger than that for H1.4 (Table S1). Therefore, the higher photocatalytic activity of H4 arises from its intrinsic structure. These results show that reaction pH can significantly influence the visible light photocatalytic activity of BiOBr for dyes in aqueous solution.

The six BiOBr samples exhibit much lower photodegradation efficiencies for MB than for RhB, in accordance with observations by Wu et al[8]. N-TiO_2 also exhibits lower photocatalytic activity for MB. Less than 60% of MB is degraded over H4 and no obvious MB degradation over N-TiO_2 is observed after irradiation for 450 min (Figs. 5b and S4). The adsorption capability of the BiOBr samples for MB is also somewhat lower than that for RhB (Figs. S5 and S4 in Supporting Information). The MB photodegradation process also does not obey the pseudo-first-order model (Fig. S5 in Supporting Information).

Specific surface area[40] and band gaps[41] are two significant factors influencing photocatalytic performance of semiconductors, which were determined using N_2 adsorption-desorption isotherms and UV-vis DRS, respectively, for the prepared BiOBr samples. All of the N_2 adsorption-desorption isotherms are of type II without hysteresis loops (Fig. S6 in Supporting Information), indicating features of nonporous materials[42]. The S_{BET}

values of H1.4, H2, H3, H4, H5 and H7 obtained by the Brunauer-Emmett-Teller (BET) method are 43.6, 93.4, 62.9, 51.7, 56.1 and 103.8 m^2/g, respectively, being within one order of magnitude (Table 1). UV-vis DRS of the BiOBr samples exhibit obvious photoabsorption from the UV to visible wavelengths shorter than 460 nm (Fig. S7 in Supporting Information). All the BiOBr samples have comparable E_g values of 2.70 ± 0.02 eV (Table 1). Similar results were reported by Zhang and coworkers for similar flaky BiOBr[24].

The six BiOBr samples have similar lamella structures, surface morphologies, band gaps and specific surface areas. The difference among them is their lamella size and thickness. Presuming the BiOBr lamellas to be circular plates, the F_{001} values of the BiOBr samples can be estimated from the equation $F_{001} = 1/(1 + 2H/L)$, as shown in Table 1. F_{001} is determined by H/L, rather than solely L. From H1.4 to H7, the trend in F_{001} is the same as those of L and H.

An increase in photoactive facet percentage and decrease in particle size can enhance the activity of photocatalysts[8, 43]. The changing tendency of photocatalytic activity from H1.4 to H7 coincides with the anticipated result from the change in H, but is opposite to that from the change of F_{001}. This indicates that for the six BiOBr samples, the effect of H on photocatalytic activity is more significant than that of F_{001}. The decrease in lamella thickness plays a key role in enhancing the photocatalytic performance of BiOBr lamellas.

Fig. 6 shows a plot of k versus H, in which a linear relationship is observed. k increases linearly with decreasing H. The formula of this linear relationship is:

$$k = -0.0020H + 0.084 \quad (3).$$

The correlation coefficient is higher than 0.99. Similar results are obtained when fitting the curves of k *vs*. D (Fig. S8 in Supporting Information). In addition, similar BiOBr lamellas with lamella thicknesses from 32 to 9 nm were synthesized by Wu and coworkers[8]. We fitted their photodegradation data for RhB to the pseudo-first-order model, and obtained k values for

their various BiOBr samples (Fig. S9a in Supporting Information). A linear relationship between *k* and lamella thickness is again obtained (Fig. S9b in Supporting Information). BiOI single-crystal nanosheets with dominant exposed (001) facets were prepared by Zan and coworkers[9]. Photocatalytic performance enhancement of prepared BiOI nanosheets was thought to be related to increasing percentage of exposed (001) facets, but meanwhile, obvious decrease of the nanosheet thickness was observed.

The above discussion indicates that decreasing the BiOBr lamella thickness is an efficient way to enhance their photocatalytic activity. Decreasing the lamella thickness decreases the bulk recombination of photoinduced electrons and holes, as they transfer by a shorter distance from the bulk to surface[43], as shown in Scheme 2. Therefore, the photocatalytic efficiency of BiOBr lamellas is strongly dependent on their thickness.

Holes, electrons, superoxide radicals ($\bullet O_2^-$) and hydroxyl radicals (•OH) are all possible active species for the photodegradation of organic pollutants[44-47]. To evaluate the role of these active species, individual scavengers were added to the photodegradation system. The scavengers used were tert-butyl alcohol for •OH[45], sodium oxalate for holes[44], $K_2Cr_2O_7$ for electrons[46] and benzoquinone for $\bullet O_2^-$ [45]. Fig. 7 shows that the addition of tert-butyl alcohol or sodium oxalate causes a slight change in the photodegradation efficiency of H4. This indicates that •OH and holes are not significant active species in the photocatalytic process. After $K_2Cr_2O_7$ is added, the photodegradation activity of H4 declines to a large extent, indicating that electrons play a role. A significant suppression of photocatalytic performance is observed when benzoquinone is added, confirming the important role of $\bullet O_2^-$ in the photodegradation process. Thus, the photocatalytic process is mainly governed by $\bullet O_2^-$, which is in agreement with the previous studies[28].

4. Conclusion

Six BiOBr lamella samples with similar lamella structures and band gaps but different

lamella sizes and thicknesses were synthesized at different pH by a hydrothermal method. The BiOBr lamella thickness can be controlled through adjusting the reaction pH. Decreasing BiOBr lamella thickness can significantly enhance their photocatalytic activity for dye degradation. Lamella thickness is more important than exposed photoactive facet content in influencing the photocatalytic activity of the BiOBr samples. Even for flaky semiconductors with high exposed photoactive facet contents, the influence of lamella thickness on photocatalytic activity should be preferentially considered.

References

1. P. Yang and J.-M. Tarascon, *Nat Mater*, 2012, **11**, 560-563.
2. M. R. Hoffmann, S. T. Martin, W. Choi and D. W. Bahnemann, *Chem Rev*, 1995, **95**, 69-96.
3. R. Asahi, T. Morikawa, T. Ohwaki, K. Aoki and Y. Taga, *Science*, 2001, **293**, 269-271.
4. Y. Zhang, Z. Chen, S. Liu and Y.-J. Xu, *Appl Catal B Environ*, 2013, **140-141**, 598-607.
5. J. G. Yu, Y. R. Su and B. Cheng, *Adv Funct Mater*, 2007, **17**, 1984-1990.
6. J. N. Wilson and H. Idriss, *J Am Chem Soc*, 2002, **124**, 11284-11285.
7. A. Hameed, T. Montini, V. Gombac and P. Fornasiero, *J Am Chem Soc*, 2008, **130**, 9658-9659.
8. D. Zhang, J. Li, Q. Wang and Q. Wu, *J Mater Chem A*, 2013, **1**, 8622-8629.
9. L. Ye, L. Tian, T. Peng and L. Zan, *J Mater Chem*, 2011, **21**, 12479-12484.
10. G. Xi and J. Ye, *Chem Commun (Camb)*, 2010, **46**, 1893-1895.
11. Y. Zheng, F. Duan, J. Wu, L. Liu, M. Chen and Y. Xie, *J Mol Catal A*, 2009, **303**, 9-14.

12. H. G. Yang, C. H. Sun, S. Z. Qiao, J. Zou, G. Liu, S. C. Smith, H. M. Cheng and G. Q. Lu, *Nature*, 2008, **453**, 638-641.

13. H. B. Jiang, Q. Cuan, C. Z. Wen, J. Xing, D. Wu, X.-Q. Gong, C. Li and H. G. Yang, *Angew Chem Int Edit*, 2011, **50**, 3764-3768.

14. S. Liu, J. Yu and M. Jaroniec, *J Am Chem Soc*, 2010, **132**, 11914-11916.

15. X. Han, Q. Kuang, M. Jin, Z. Xie and L. Zheng, *J Am Chem Soc*, 2009, **131**, 3152-3153.

16. G. Liu, H. G. Yang, X. Wang, L. Cheng, J. Pan, G. Q. Lu and H.-M. Cheng, *J Am Chem Soc*, 2009, **131**, 12868-12869.

17. Y. Bi, S. Ouyang, N. Umezawa, J. Cao and J. Ye, *J Am Chem Soc*, 2011, **133**, 6490-6492.

18. L. Ye, L. Zan, L. Tian, T. Peng and J. Zhang, *Chem Commun*, 2011, **47**, 6951-6953.

19. S. Xie, X. Han, Q. Kuang, J. Fu, L. Zhang, Z. Xie and L. Zheng, *Chem Commun*, 2011, **47**, 6722-6724.

20. C. Z. Wen, J. Z. Zhou, H. B. Jiang, Q. H. Hu, S. Z. Qiao and H. G. Yang, *Chem Commun*, 2011, **47**, 4400-4402.

21. C. Z. Wen, H. B. Jiang, S. Z. Qiao, H. G. Yang and G. Q. Lu, *J Mater Chem*, 2011, **21**, 7052-7061.

22. X. Huang, Y. Li, Y. Li, H. Zhou, X. Duan and Y. Huang, *Nano Letters*, 2012, **12**, 4265-4270.

23. H. Liu, M. Luo, J. Hu, T. Zhou, R. Chen and J. Li, *Appl Catal B Environ*, 2013,

140-141, 141-150.

24. J. Wang, Y. Yu and L. Zhang, *Appl Catal B Environ*, 2013, **136-137**, 112-121.

25. K. Zhang, J. Liang, S. Wang, J. Liu, K. Ren, X. Zheng, H. Luo, Y. Peng, X. Zou, X. Bo, J. Li and X. Yu, *Cryst Growth Des*, 2011, **12**, 793-803.

26. X. Zhang, Z. Ai, F. Jia and L. Zhang, *J Phys Chem C*, 2008, **112**, 747-753.

27. Y. F. Fang, W. H. Ma, Y. P. Huang and G. W. Cheng, *Chem Eur J*, 2013, **19**, 3224-3229.

28. Y. Huo, J. Zhang, M. Miao and Y. Jin, *Appl Catal B Environ*, 2012, **111-112**, 334-341.

29. J. Xu, W. Meng, Y. Zhang, L. Li and C. Guo, *Appl Catal B Environ*, 2011, **107**, 355-362.

30. H. Cheng, B. Huang, Z. Wang, X. Qin, X. Zhang and Y. Dai, *Chem Eur J*, 2011, **17**, 8039-8043.

31. H. Gnayem and Y. Sasson, *ACS Catalysis*, 2013, **3**, 186-191.

32. J. Fu, Y. Tian, B. Chang, F. Xi and X. Dong, *J Mater Chem*, 2012, **22**, 21159-21166.

33. J. Wang and Y. Li, *Chem Commun*, 2003, 2320.

34. H. Deng, J. Wang, Q. Peng, X. Wang and Y. Li, *Chem Eur J*, 2005, **11**, 6519-6524.

35. Q. Li, B. Guo, J. Yu, J. Ran, B. Zhang, H. Yan and J. R. Gong, *J Am Chem Soc*, 2011, **133**, 10878-10884.

36. M. Shang, W. Wang and L. Zhang, *J Hazard Mater*, 2009, **167**, 803-809.

37. W. L. Huang and Q. Zhu, *J Comput Chem*, 2009, **30**, 183-190.

38. M. Zhang, C. Shao, J. Mu, X. Huang, Z. Zhang, Z. Guo, P. Zhang and Y. Liu, *J Mater*

Chem, 2012, **22**, 577-584.

39. S. Ye, L.-G. Qiu, Y.-P. Yuan, Y.-J. Zhu, J. Xia and J.-F. Zhu, *J Mater Chem A*, 2013, **1**, 3008-3015.

40. Q. Xiang, B. Cheng and J. Yu, *Appl Catal B Environ*, 2013, **138-139**, 299-303.

41. E. W. McFarland and H. Metiu, *Chem Rev*, 2013, **113**, 4391-4427.

42. D. H. Everett, *Pure Appl Chem*, 1986, **58**, 967-984.

43. Z. Zhang, C.-C. Wang, R. Zakaria and J. Y. Ying, *J Phys Chem B*, 1998, **102**, 10871-10878.

44. X. Xiao, R. Hu, C. Liu, C. Xing, C. Qian, X. Zuo, J. Nan and L. Wang, *Appl Catal B Environ*, 2013, **140-141**, 433-443.

45. L. Mohapatra, K. Parida and M. Satpathy, *J Phys Chem C*, 2012, **116**, 13063-13070.

46. S. Ge and L. Zhang, *Environ Sci Technol*, 2011, **45**, 3027-3033.

47. Q. Xiang, J. Yu and P. K. Wong, *J Colloid Interface Sci*, 2011, **357**, 163-167.

Graphical abstract

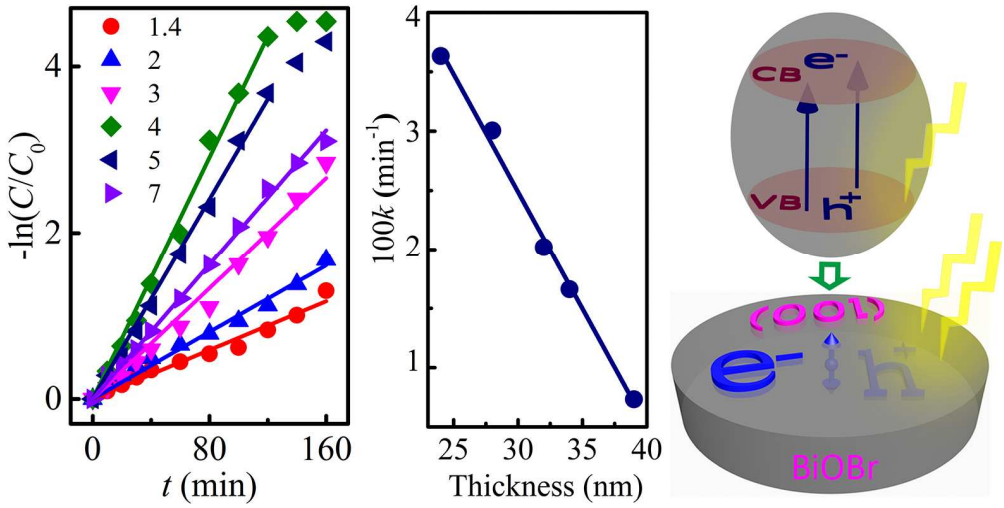

Photocatalytic activity of BiOBr samples is enhanced by more than four times by adjusting the reaction pH.

Figure and table captions

Fig. 1 XRD patterns of as-prepared BiOBr samples.

Fig. 2 SEM images of the BiOBr samples H1.4□H7, shown in a□f, respectively. Insets indicate lamella thickness of samples.

Fig. 3 (a) TEM, (b and c) HRTEM and (d) SAED images of BiOBr sample H4.

Fig. 4 Survey scan and high-resolution XPS spectra of the Bi 4f, Br 3d and O 1s regions for BiOBr samples.

Fig. 5 Photodegradation of BiOBr samples for (a and c) RhB and (b) MB, under visible light irradiation.

Fig. 6 Dependence of pseudo-first-order rate constant (*k*) on lamella thickness of BiOBr samples.

Fig. 7 Photocatalytic degradation of RhB over the BiOBr sample H4 with different scavengers: 20 mM tert-butyl alcohol (*t*-BuOH), 0.2 mM sodium oxalate, 10 mM $K_2Cr_2O_7$ and 0.1 mM benzoquinone.

Scheme 1 Structural model illustration of BiOBr crystals (3×3×3 lattices), showing (a) three-dimensional projection, (b) (001) facets, (c) (010) facets and (d) (100) facets.

Scheme 2 Schematic showing separation of a photoinduced electron (e^-) and hole (h^+), and transfer from the bulk to surface of BiOBr lamellas.

Table 1 Physicochemical properties and photocatalytic activities of BiOBr samples.

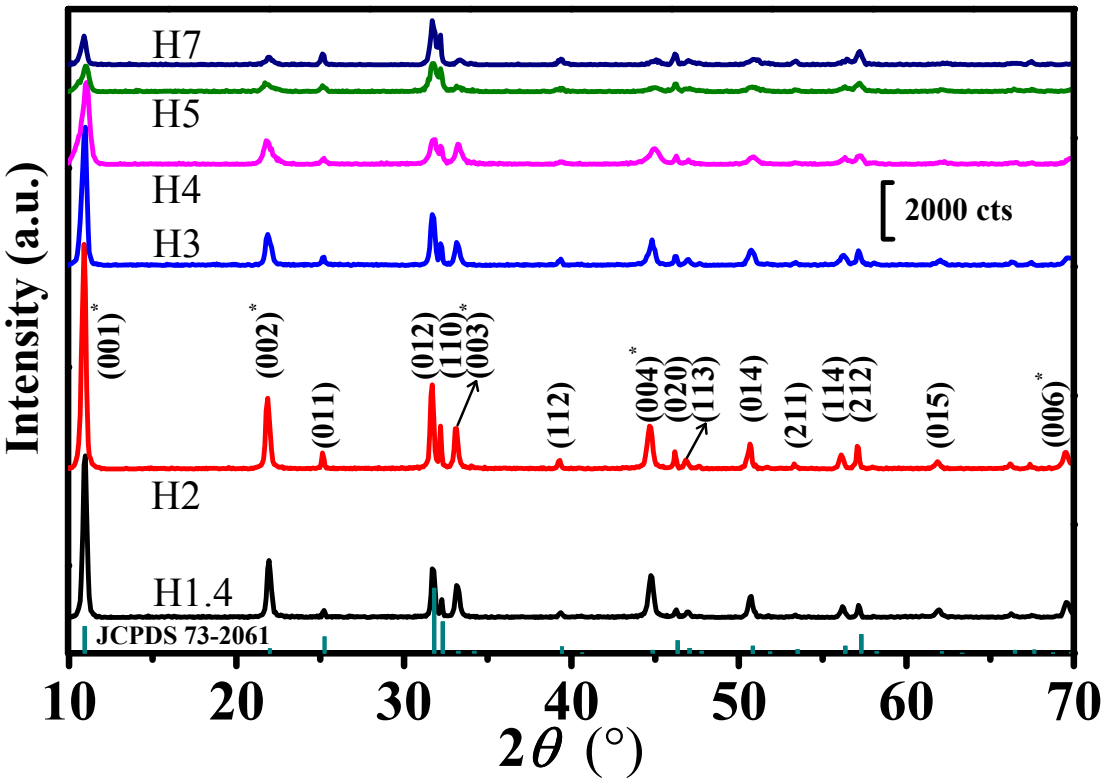

Fig. 1 XRD patterns of as-prepared BiOBr samples.

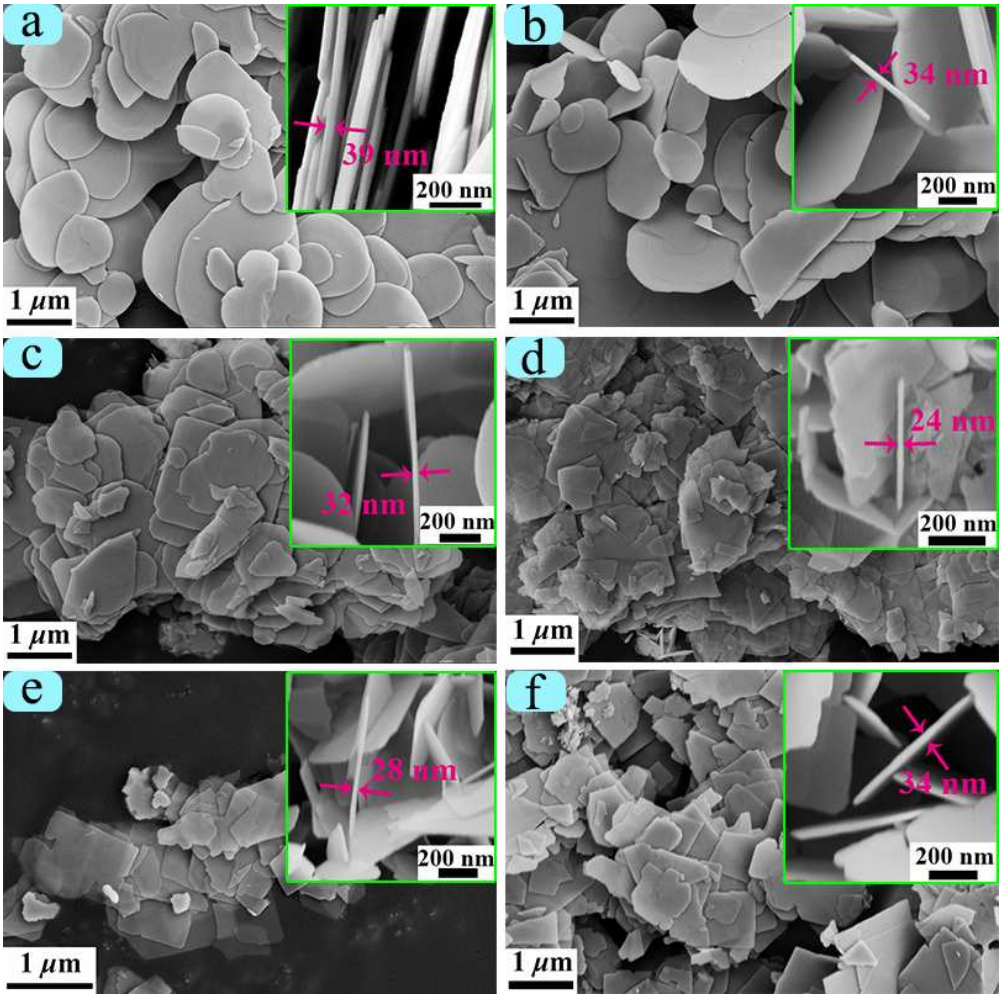

Fig. 2 SEM images of the BiOBr samples H1.4□H7, shown in a□f, respectively. Insets indicate lamella thickness of samples.

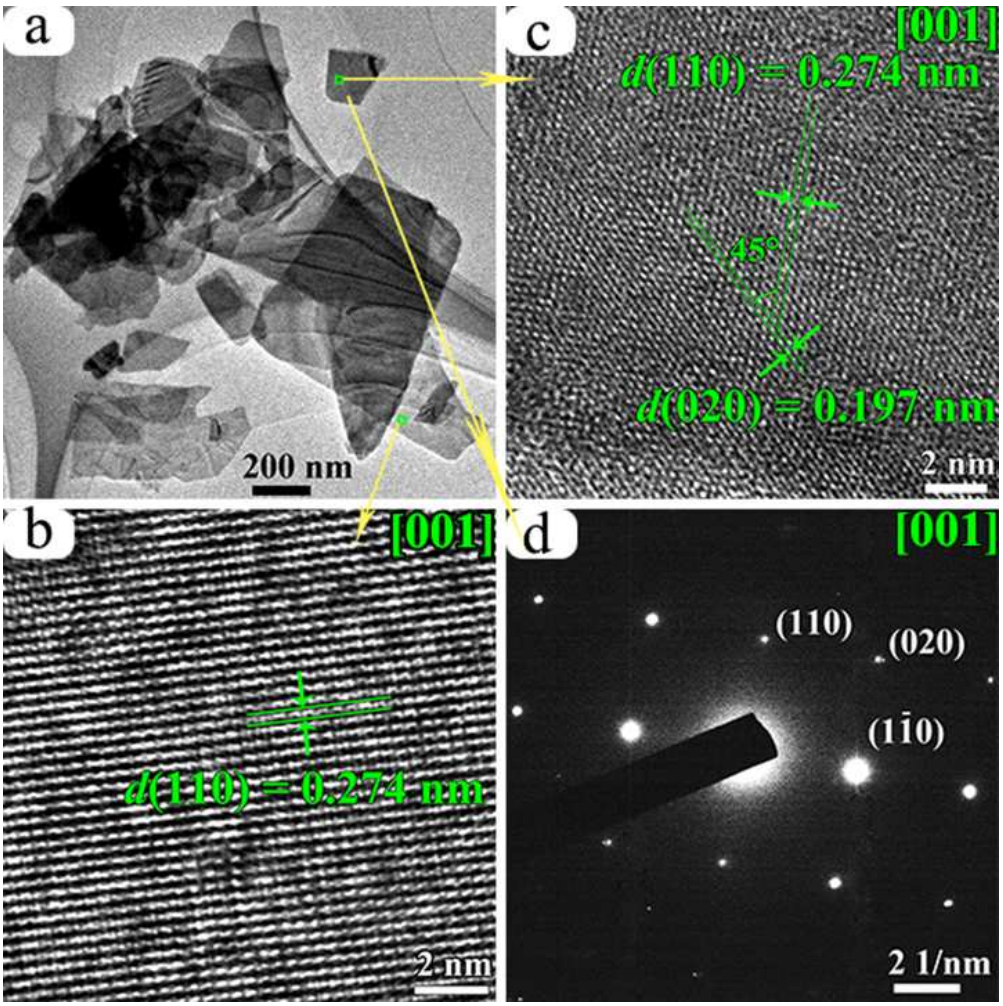

Fig. 3 (a) TEM, (b and c) HRTEM and (d) SAED images of BiOBr sample H4.

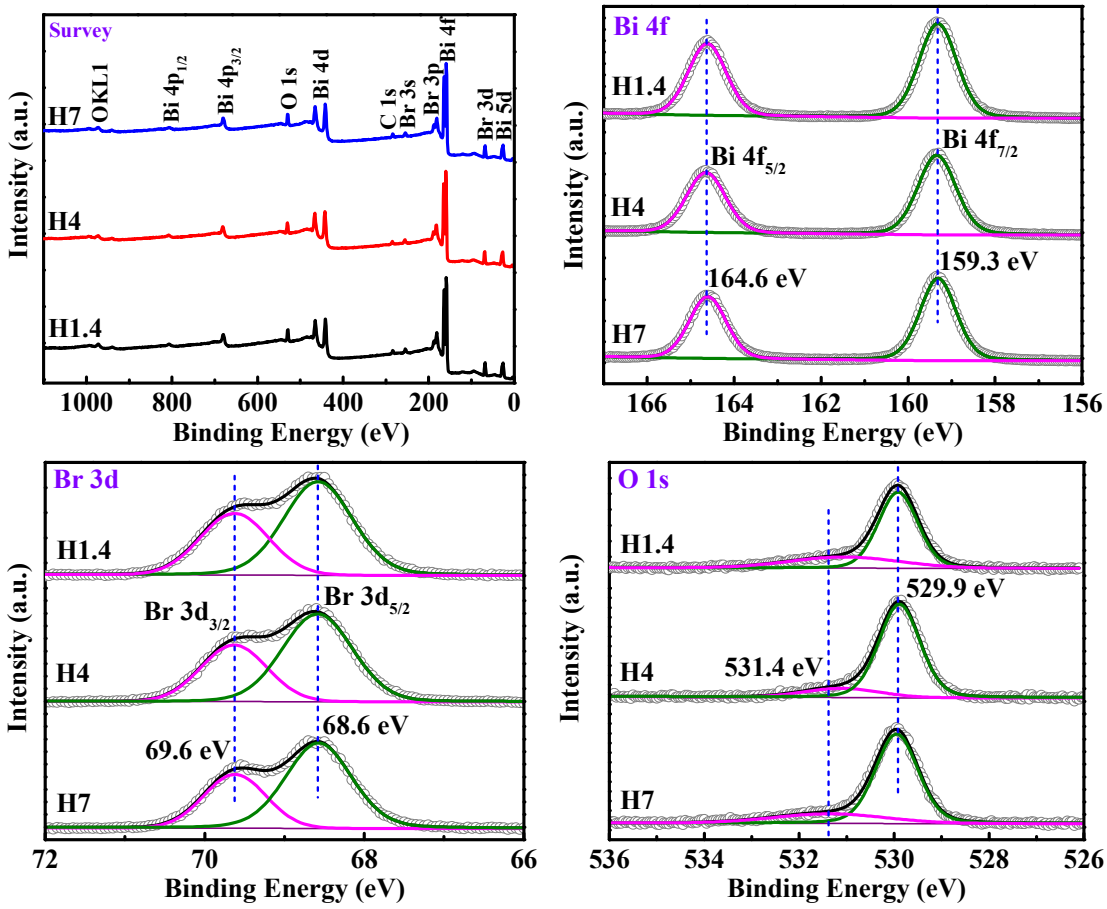

Fig. 4 Survey scan and high-resolution XPS spectra of the Bi 4f, Br 3d and O 1s regions for BiOBr samples.

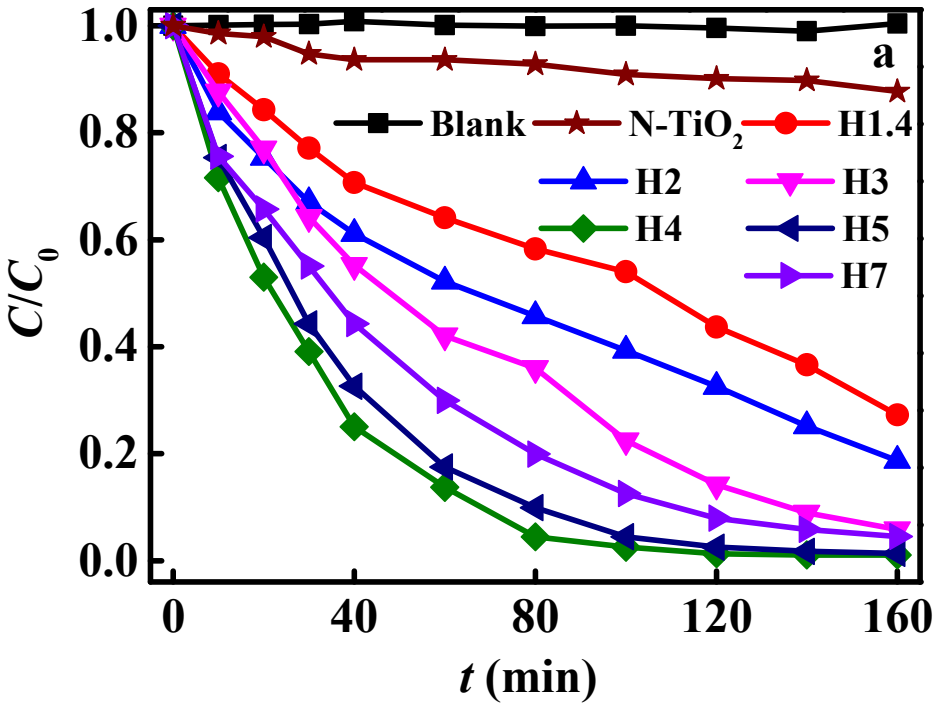

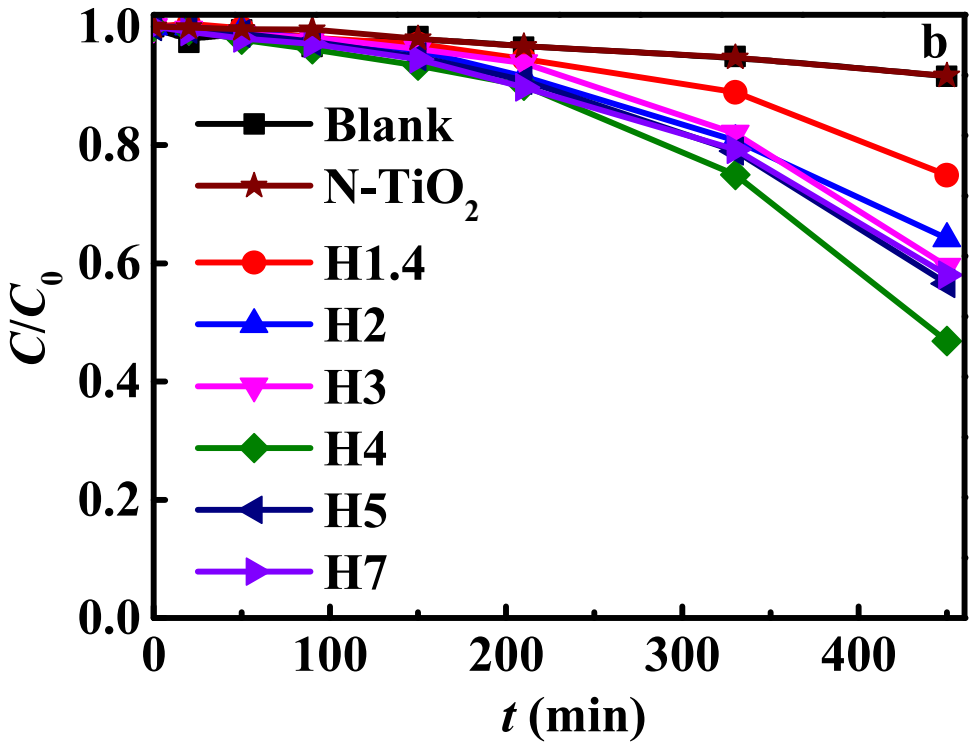

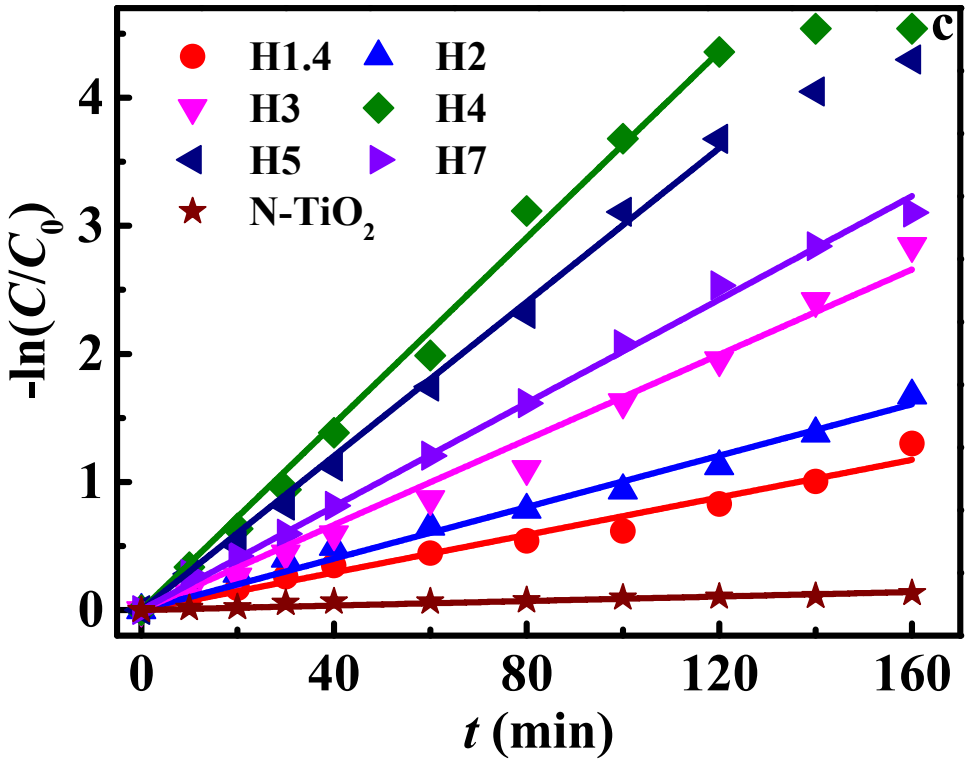

Fig. 5 Photodegradation of BiOBr samples for (a and c) RhB and (b) MB, under visible light irradiation.

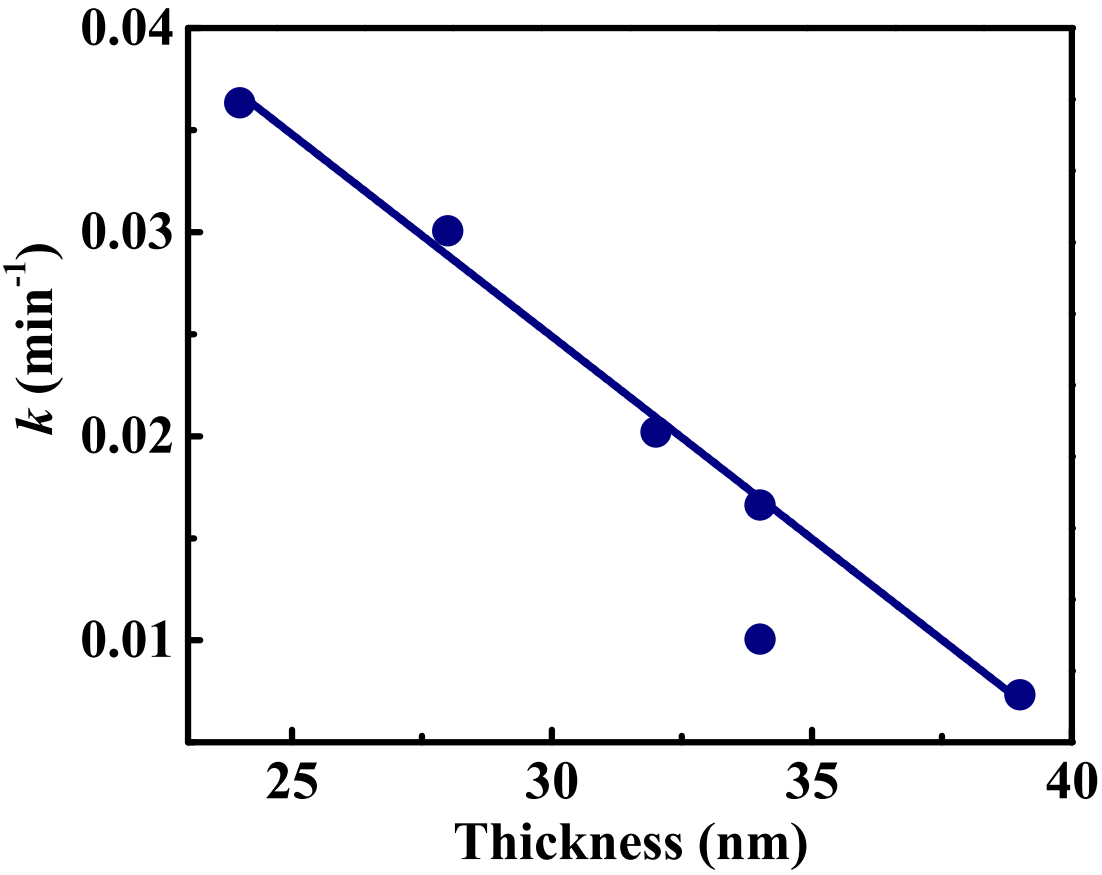

Fig. 6 Dependence of pseudo-first-order rate constant (k) on lamella thickness of BiOBr samples.

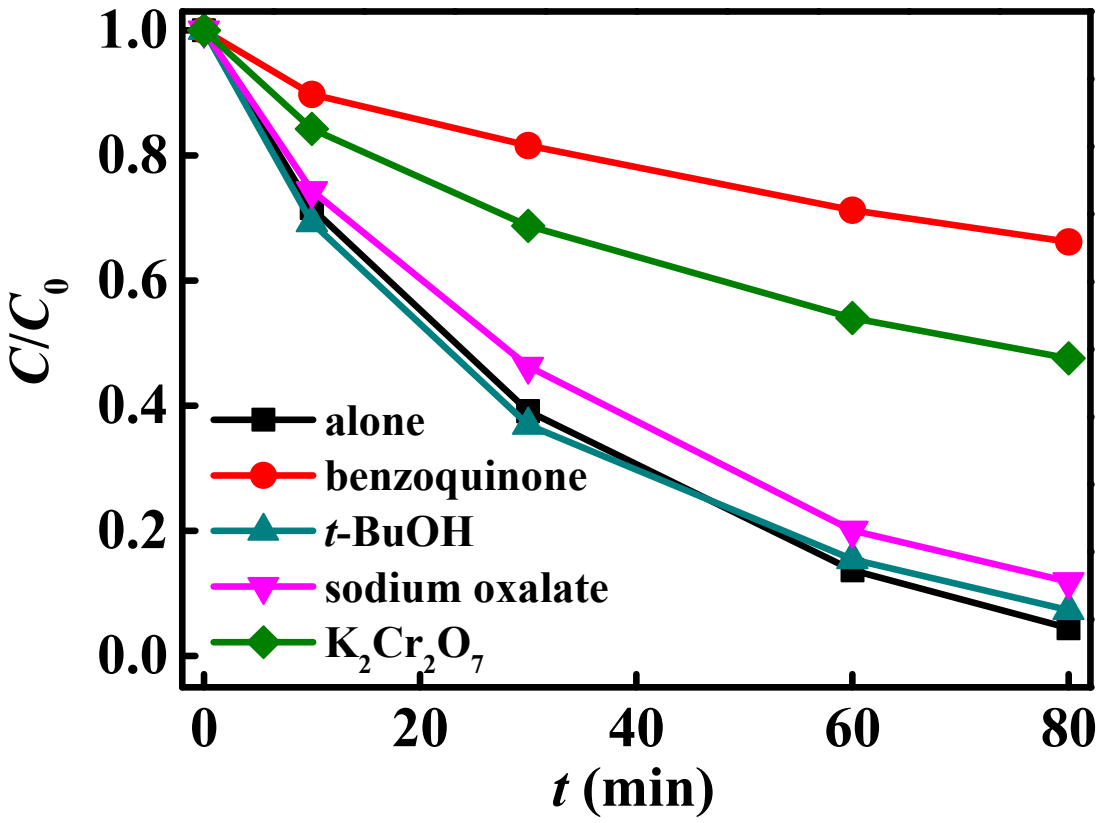

Fig. 7 Photocatalytic degradation of RhB over the BiOBr sample H4 with different scavengers: 20 mM tert-butyl alcohol (*t*-BuOH), 0.2 mM sodium oxalate, 10 mM $K_2Cr_2O_7$ and 0.1 mM benzoquinone.

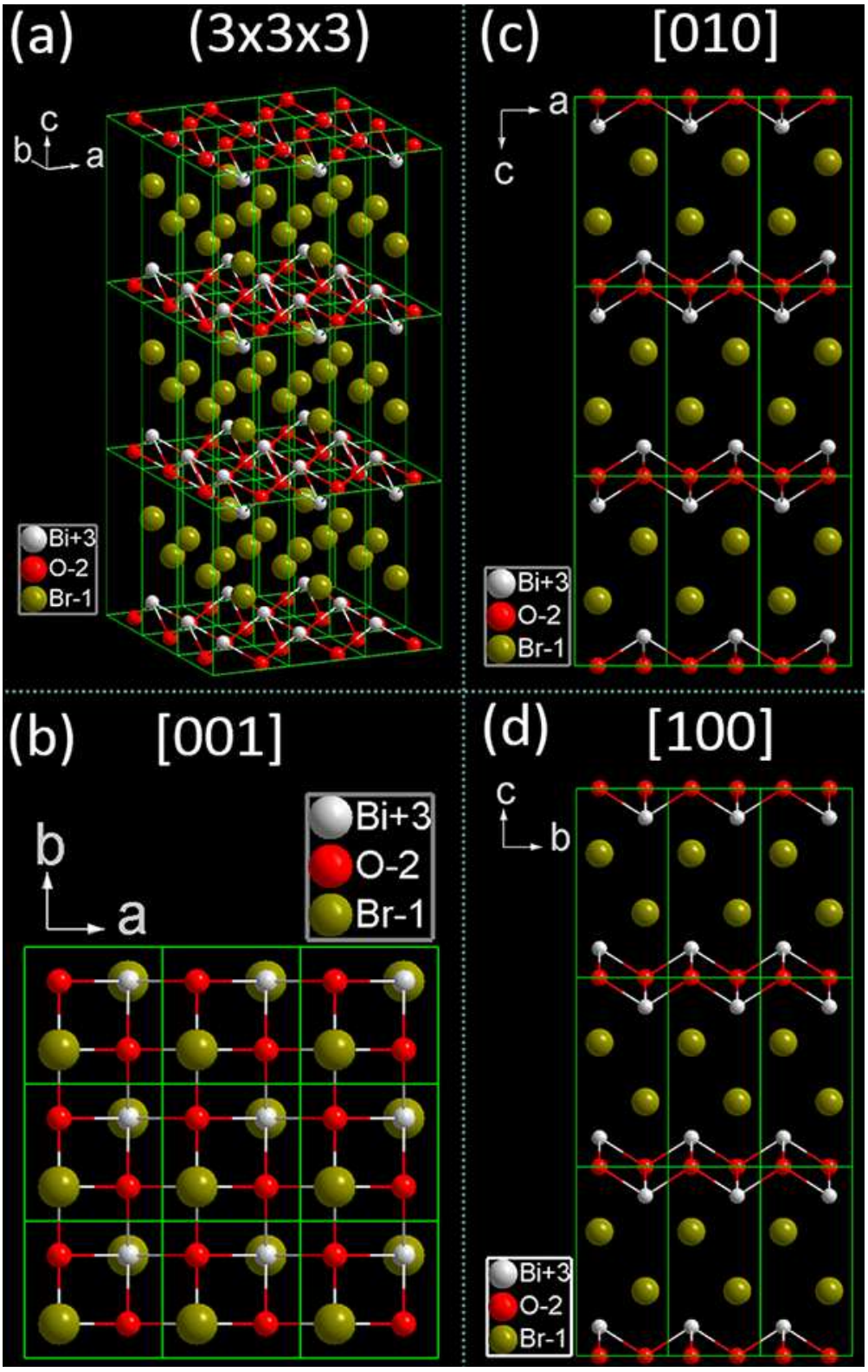

Scheme 1 Structural model illustration of BiOBr crystals (3×3×3 lattices), showing (a) three-dimensional projection, (b) (001) facets, (c) (010) facets and (d) (100) facets.

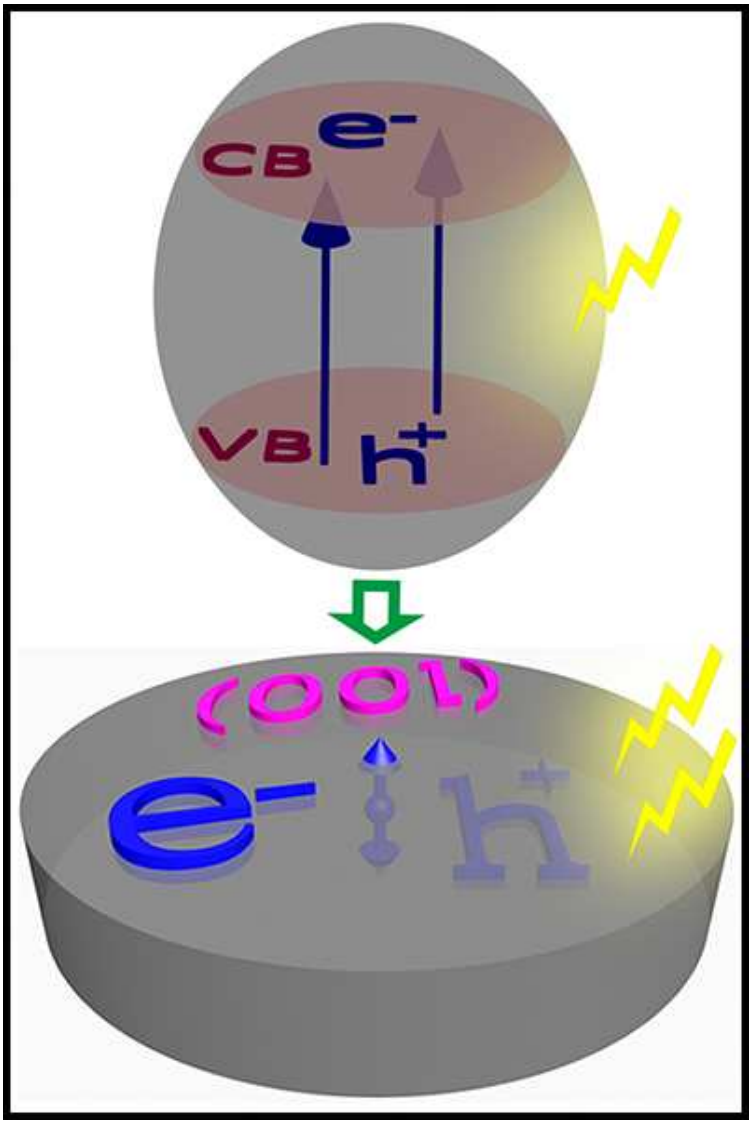

Scheme 2 Schematic showing separation of a photoinduced electron (e^-) and hole (h^+), and transfer from the bulk to surface of BiOBr lamellas.

Table 1 Physicochemical properties and photocatalytic activities of BiOBr samples.

Sample	Reaction pH	D^a (nm)	H^b (nm)	L^c (nm)	$H_A{}^d$ (nm)	S_{BET} ($m^2 g^{-1}$)	E_g (eV)	$k^e \times 10^3$ (min^{-1})	$F_{001}{}^f$ (%)
H1.4	1.4	42	39	963	46	43.6	2.72	7.33	92.5
H2	2.0	39	34	935	44	93.4	2.72	10.05	93.2
H3	3.0	36	32	389	33	62.9	2.71	16.62	85.9
H4	4.0	21	24	230	23	51.7	2.71	36.33	82.7
H5	5.0	23	28	391	28	56.1	2.69	30.06	87.5
H7	7.0	32	34	554	38	103.8	2.68	20.20	89.1

[a] Crystallite size calculated by Scherrer formula from (001) plane.

[b] Lamella thickness from SEM images.

[c] Average size of BiOBr lamellas from SEM images.

[d] Lamella thickness from SEM images.

[e] The degradation rate constant of RhB over BiOBr photocatalysts.

[f] Percentage of exposed (001) facets.